DOI: https://dx.doi.org/10.4314/gjgs.v21i1.9

GLOBAL JOURNAL OF GEOLOGICAL SCIENCES VOL. 21, 2023: 129-142
COPYRIGHT© BACHUDO SCIENCE CO. LTD PRINTED IN NIGERIA ISSN 1596-6798
www.globaljournalseries.com.ng, Email: globaljournalseries@gmail.com

STRUCTURAL LINEAMENT MAPPING USING REMOTE SENSING IN THE AURES MASSIF (NE ALGERIA)

RAMI DJEFFAL, MOHAMED CHADI AND EL HADJ YOUCEF BRAHIM

(Received 20 December 2022; Revision Accepted 27 December 2022)

ABSTRACT

The Aures massif is located in the eastern part of the Atlasic Domain and formed by Mesozoic and Cenozoic sedimentary rocks. The main objective of this study is to map the structural lineaments and geologically analyze their different geometric aspects, like orientation and distribution, using remote sensing data. Another important aim is to track the extent of lineaments, understand how they integrate into the regional structure and trace the main tectonic events responsible for the Aures' structuration. Both manual and automatic approaches were employed to achieve the study's objectives. More than twelve thousand lineaments were identified, and grouped into four direction families: NW-SE, NE-SW, E-W, and N-S. Two main factors control the orientation: density and distribution of the lineaments, and topographic and geologic factors. A good correspondence was found between literature and techniques employed in this work regarding structural lineament analysis showing that the Aures lineaments result from the succession of Alpine orogeny tectonic phases. Mainly two phases were responsible on its structuration: the major Atlasic event, which occurred during the Lutetitian stage with NW-SE trending, and the Alpine which happened in late Miocene with N-S compression.

INTRODUCTION

Many authors emphasized the importance of lineament mapping as part of various geological investigations (e.g. Mwaniki et al., 2015; Ramli et al., 2010). Lineament extraction can help interpret the regional structure of a given area and discern its different structural elements (Abdelouhed et al., 2022; Bentahar et al., 2020; Fossi et al., 2021). Lineaments can also assist in understanding underlying rocks architecture (e.g. basement faults), exploring mineral deposits (Adepoju et al., 2021; Hubbard et al., 2012; Liu et al., 2000), and discovering groundwater reservoirs (Al-Saedi, 2013; Bruning et al., 2011; Saint Jean Patrick Coulibaly et al., 2020). According to Hobbs (1904), lineaments correspond to morphological structures, generally rectilinear, and may be described as "(1) crests of ridges or the boundaries of elevated areas (2) drainage lines (3) coast lines, and (4) boundary lines of geological formations of petrographic rock types, or of lines of outcrops". Later, Hobbs (1912) completed this definition by adding "ravines or valleys and visible lines of fracture or zones of fault breccia". Several definitions then followed to include more earth linear features (O'Leary et al., 1976). The description given by Benabbas (2006) was retained, defining the lineaments as rectilinear or slightly curved structures that appear in landscape and which may correspond either to physiographic features linked to vegetation, hydrography, or morphology: ridges, relief limits, outcrop lines, or to elements of structural origin: faults, reversals of layers, a dense network of joints. Genetically, the lineaments can result from geological (e.g., faults, fractures, joints), morphological (e.g., stream channels, drainage divides, ridges), or anthropogenic processes (e.g., roads or field boundaries) (Adhab, 2014; Soliman & Han, 2019). The lineaments can also reflect deep structures (flexures, basement faults, deep folds).

In digital image processing, lineaments usually occur as edges with tonal differences. Most extraction techniques are based on edge enhancement by

Rami Djeffal, Frères Mentouri Constantine 1 University, Constantine, Algeria
Mohamed Chadi, Salah Boubnider Constantine 3 University, Constantine, Algeria.
El Hadj Youcef Brahim, Chahid Mustapha Ben Boulaïd Batna 2 University, Batna, Algeria.

improving the tone, the hue, and the image structure (Hung et al., 2005; Javhar et al., 2019). In this regard, two methods are proposed for identifying and extracting lineaments from remote sensing data: manual and automatic. The manual method consists of enhancing the tonal differences, then visually interpreting the lineament segments of the satellite image. This technique is efficient but it is relatively time-consuming and more importantly highly subjective. The automatic method uses computer software and algorithms to detect and extract lineaments automatically. Although this technique is quick, it generates many insignificant lineaments and must go through a post-processing phase that includes validation and removing anthropic lineaments. As a result, some manual processing should be incorporated (Abdelouhed et al., 2022). However, Ahmadi and Pekkan (2021) proposed that a single method may not provide an accurate lineament distribution. It is therefore necessary that the identification and extraction of lineaments integrate automatic and manual methods.

This study is the first structural study applying remote sensing (Landsat 9, Sentinel 2 and SRTM) data on the Aures Massif. The latter forms an excellent choice, due to its well-exposed geologic formations, overall low-density vegetal cover, and the lack of recent literature. Moreover, the Aures has a well-developed fracturing network and extends over a large geographic area with several hard-to-reach locations. Another aim of this study is to describe the important structural events that affected the Aures throughout its geological history and retrace their chronology based on the different lineaments' sets directions.

Geographical and geological setting

The Aures Massif is situated in the northeast part of Algeria, lying between 34°48' and 35°34'N Latitudes and 5°34' and 7°09'E Longitudes. The Aures is bordered in the north by the Timgad Basin and the Batna-Aïn Touta plain, in the south by the Chott Melrhir steppe, in the west by Oued El Haï valley followed by El Outaya plain, and in the east by Oued El Arab valley (Fig. 1). The study area is located in the eastern part of the Atlasic Domain, belonging to the foreland of the North African Alpine Belt (Bouillin, 1986; Domzig, 2006; Durand Delga, 1969; Raoult & JF, 1974).

The lithological series of the Aures is characterized by thick sedimentary sets extending over the Mesozoic and the Cenozoic. However, the Cenozoic outcrops are relatively less developed compared to Mesozoic ones. The study of the Aures Massif lithostratigraphic series is due to (Benmansour et al., 2018; Bensekhria et al., 2019; Djaiz, 2011; Ghandriche, 1991; Herkat, 1999; Laffite, 1939; Yahiaoui, 1990) and it is formed by (Fig. 2):

The Triassic, which forms the most ancient rocks in the study area. It is always found in abnormal stratigraphic positions, either in the form of diapirs piercing secondary and tertiary strata or injected along with tectonic accidents within surrounding rocks.

The Jurassic outcrops are localized only at the center of two Aures massif anticlines; one can distinguish: the Lower Jurassic, located in the northwest part of the Aures near Menâa region at the east of Djebel Haouidja, consisting of fossiliferous shales with ammonites of Toarcian, and the Upper Jurassic which is located at the center of Djebel El Azereg anticline at the southeast of lower Jurassic outcrops, represented by Kimmeridgian and Tithonian, formed mainly by carbonate rocks (limestone and dolomite).

The Cretaceous is widely represented in the Aures Massif and forms the most developed outcrops by showing a concordant series where all stages are present. The Aures's Cretaceous exhibits an evident opposition between two successive series: the first corresponds to Lower Cretaceous, with sandstone dominating. In contrast, the second one corresponds to Upper Cretaceous, where sandstones are missing.

The Paleogene is well represented in the Aures, located in big synclines and the South Saharan Flexure (SSF); two sets form the Paleogene: at the bottom, a fossiliferous marine set (Danian- Upper Lutetian), and at the top an azoic continental set (Upper Eocene- Oligocene).

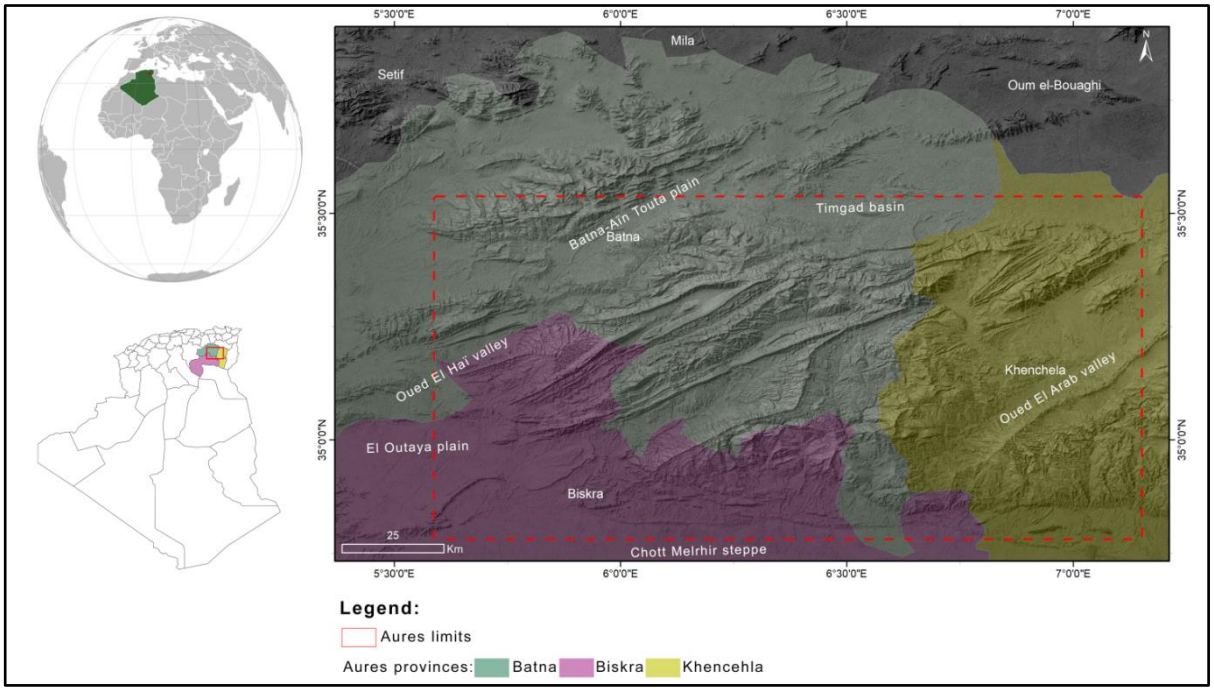

Fig. 1 Geographic location of the Aures Massif

The Neogen main outcrops are identified at the Aures borders, composed of detrital rocks where clays are dominant. The Neogen series often rest in discordance with formations of different ages (Oligocene, Eocene, Upper Cretaceous), containing several lithostratigraphic sets forming sequences whose boundaries are often heterochronous.

From a structural point of view, six vast northwest-southeast oriented folds forming the Aures southward were distinguished (Ghandrish,1991): (i) Anticline axis of Djebel Ahmer, Djebel Metlili, Djebel Ich Ali (ii) Anticline axis of Djebel Mérkizane, Djebel Haouidja, Igguedelène, (iii) Bouzina syncline; (iv) Anticline axis of Djebel Azreg, Djebel Ichmoul, Djebel Chelia, (v) Rhassira syncline; (vi) Anticline axis of Djebel Taktiout, Djebel Toubount; Djebel Khenchela. These vast folds are cross-cut by a dense multidirectional faults network.

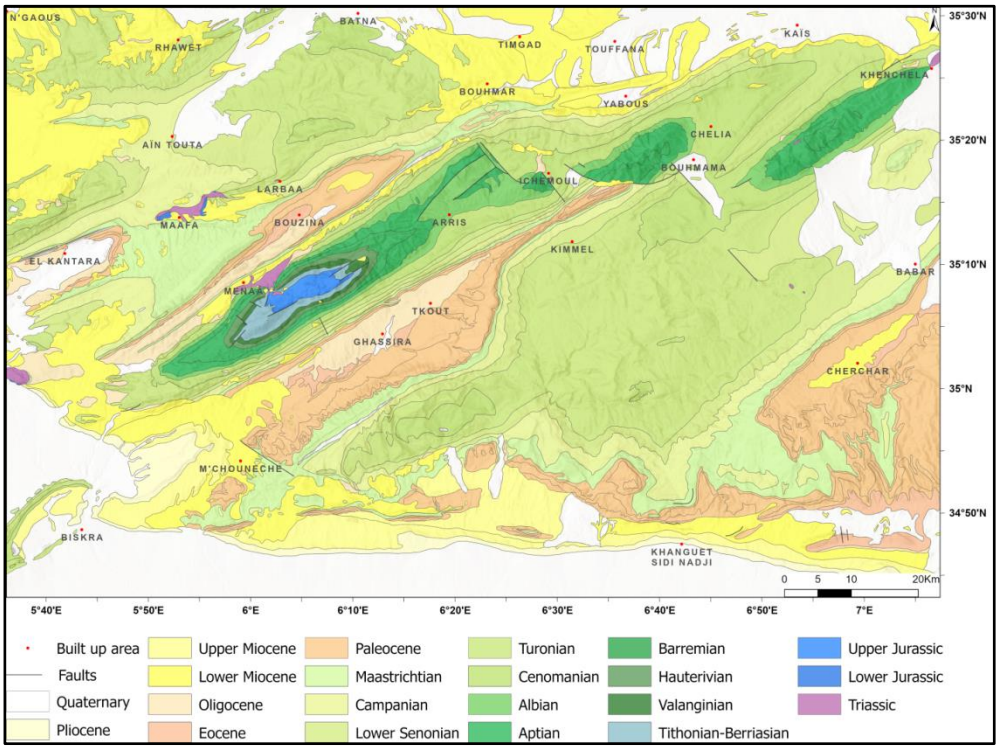

Fig. 2 Geologic map of the Aures Massif modified from Laffite (1939)

METHODOLOGY

The methodology followed in this study is as shown on Fig. 3.

Data collection

Two datasets were used: multispectral images and Digital Elevation Models (DEMs).

***Multispectral images*:** produced using sensors that capture and measure reflected energy within a specific range of wavelengths under different resolutions (Table 1). Two multispectral images from three satellites were employed.

Landsat 9, a collaboration between the National Aeronautics and Space Administration (NASA) and the United States Geological Survey (USGS). To cover the Aures Massif four scenes were used (Table 2), each scene comprises 11 bands, but for the aim of this study, we have used the seven bands (1 to 7) with 30 m resolution each (Table 1).

Sentinel-2, developed and operated by the European Space Agency (ESA). Bands 2 to 8 and 11 to 12 were used (Table 1). With higher resolution, six scenes were needed to cover the Aures Massif (Table 2).

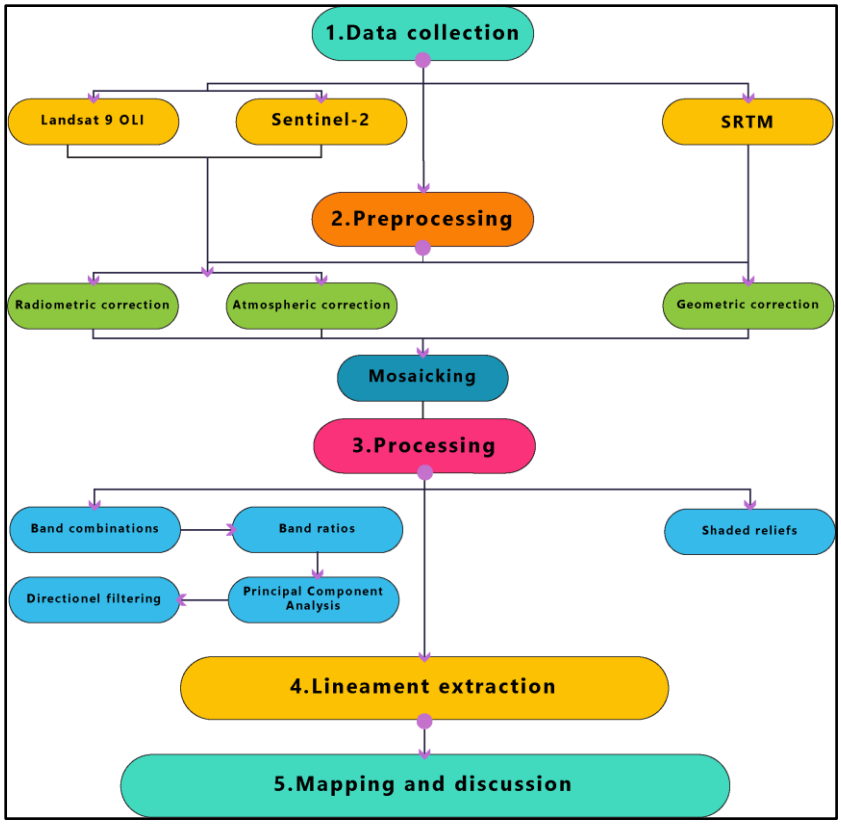

Fig. 3 Methodology flowchart

Both multispectral image datasets were downloaded from the USGS Earth Explorer website, considering periods with less vegetation, snow, and clouds.

Table 1: Bands of Landsat 9 and Sentinel-2A multispectral images **OLI:** Operation Land Imager, **NIR:** Near-Infrared, **SWIR:** Short Wave Infrared, **TIRS:** Thermal Infrared

Landsat 9 OLI/TIRS				**Sentinel 2**			
	Bands	Central wavelength (µm)	Resolution (m)		Bands	Central wavelength (µm)	Resolution (m)
1	Coastal Aerosol	0.440	30	1	Coastal Aerosol	0.443	60
2	Blue	0.480	30	2	Blue	0.490	10
3	Green	0.560	30	3	Green	0.560	10
4	Red	0.655	30	4	Red	0.665	10
5	NIR	0.865	30	5	Vegetation Red Edge	0.705	20
6	SWIR 1	1.610	30	6	Vegetation Red Edge	0.740	20
7	SWIR 2	2.20	30	7	Vegetation Red Edge	0.783	20
8	Panchromatic	0.590	15	8	NIR	0.842	10
9	Cirrus	1.370	30	8A	Narrow NIR	0.865	20
10	TIRS 1	10.895	100	9	Water vapor	0.945	60
11	TIRS 2	12.005	100	10	SWIR-Cirrus	1.375	60
				11	SWIR 1	1.610	20
				12	SWIR 2	2.190	20

Digital Elevation Model (DEM), Digital Elevation Models are arrays of regularly distributed elevation values -altitudes- referenced to various projection systems. The Digital Elevation Model used in this study is extracted from Shuttle Radar Topographic Mission (SRTM) data with a resolution of 1 arc-second (30 m), globally available to download from the USGS Earth Explorer website.

Table 2 Mosaicked scenes and their date of acquisition

Landsat 9			**Sentinel 2**		
	Scene path/row	Date of acquisition	Scene	Date of acquisition
1	193/35	June 24, 2022	1 T31SGV	July 05, 2021
2	193/36	June 24, 2022	2 T32SKE	August 24, 2021
3	194/35	June 15, 2022	3 T32SLE	August 06, 2021
4	194/36	June 15, 2022	4 T31SGU	December 07, 2021
			5 T32SKD	November 10, 2021
			6 T32SLD	December 04, 2021

Preprocessing

The necessary preprocessing phase consists of applying radiometric and atmospheric corrections on multispectral images, while the SRTM data was geometrically corrected to assure perfect superposition. The mosaicking of different scenes from (Table 1) is performed at this phase using Envi Exelis software.

Processing

The issued multispectral images from the preprocessing phase were served for:

Band combinations: Each band of the used multispectral images (Table 1) can be individually displayed as a grayscale image (Fig. 4a), or it can be combined with two other bands to form a color composite image (Fig. 4b).

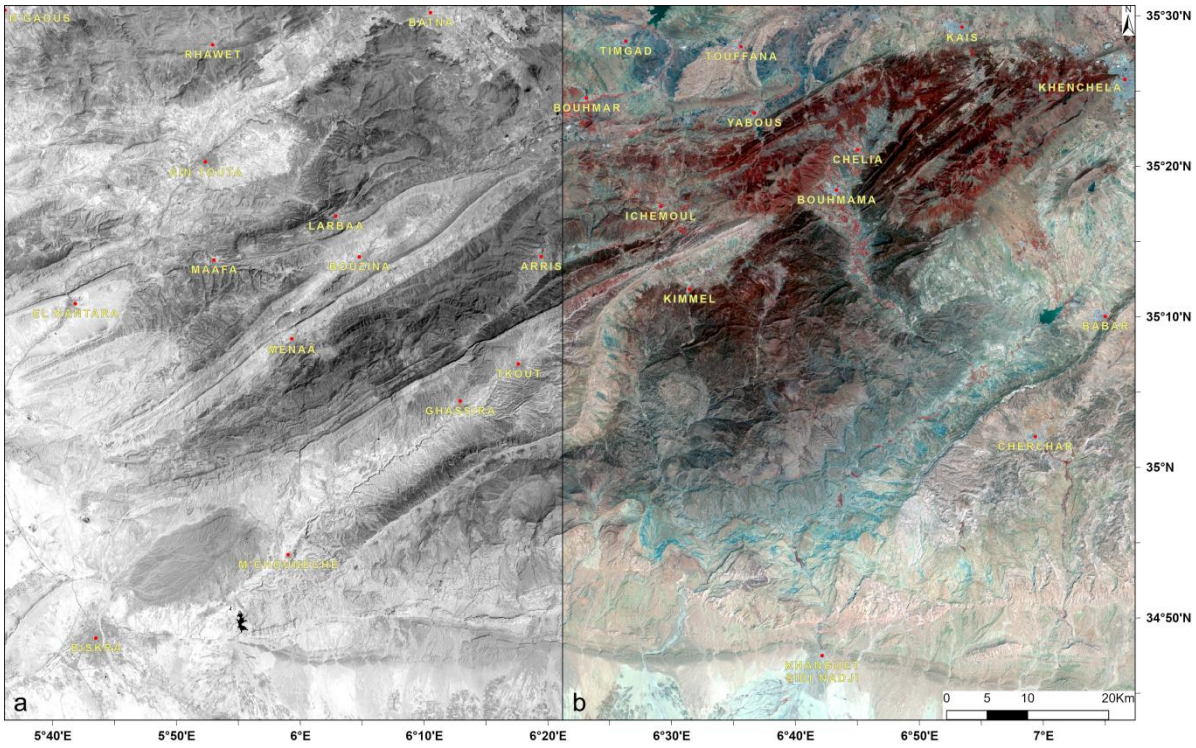

Fig. 4 a: Grayscale image of Landsat 9 Band 5 **b:** RGB-532 band combination of Landsat 9

SWIR 2, SWIR 1, and blue corresponding respectively to RGB is a particularly useful combination for identifying lithological formations and faults (7 6 2 for Landsat 9 and 12 11 2 for Sentinel-2).

Band ratioing: The band ratioing technique can be used to enhance the spectral differences between bands. Just as the data in an image can be displayed as grey-tone images of single bands or as RGB three-band color images, various arithmetic combinations of bands can also be used. The most useful of these is the ratio of one band to another. It is prepared simply by dividing the DN (Digital Number) of each pixel in one band by that for the corresponding pixel in another band. Theoretically, this should produce a range of new values for the pixel from zero to infinity (Drury, 2001). Thus, combinations (4/3, 6/2, 7/5), (4/3, 6/2, 7/4), and (5/4,7/3, 7/4) for Landsat 9 and their equivalent for Sentinel 2 were found to have the best contrast.

Principal Component Analysis (PCA): The PCA is also called principal components transformation. It is commonly used in geology for lineament extraction (e.g., Adiri et al., 2017; Khalifa et al., 2021; Salui, 2018). It is a well-known mathematical technique that characterizes a large number of variables into a new smaller set without losing a significant amount of original information. Multispectral images like Landsat 9 OLI and Sentinel 2 have numerous spectral bands (Table 1) and frequently contain redundant data. PCA allows us to remove these redundancies (Canty, 2014; Chuvieco, 2020). The outcome of this processing phase from ENVI software is multiple images (PC1, PC2…etc.). The covariance table obtained from PCA shows that most information is concentrated in PC1: 93.64% for Landsat-9 and 94.93% for Sentinel-2, which will be used for further processing.

Directional filtering is a multi-purpose technique commonly used to sharpen the image for edge detection and selective linear enhancement. This technique is useful in structural geology for improving linear structures such as faults and fractures and for general manual lineament extraction. In our work, we have used a 7x7 matrix in seven directions (0^o, $N45^o$, $N90^o$, $N135^o$) on PC1 obtained from the principal component analysis. Each result enhances a different line direction.

Multidirectional shaded relief or hill-shading is the basic technique to create an intuitive and easy-to-interpret 3D impression of the terrain and should be used for its cartographic consistencies (Tzvetkov, 2018). For our study, we have used four shaded relief images with a solar azimuth of 0°, 45°, 90°, and 135° maintaining solar elevation at 45° and under three color modes: grey, red and hypsometric.

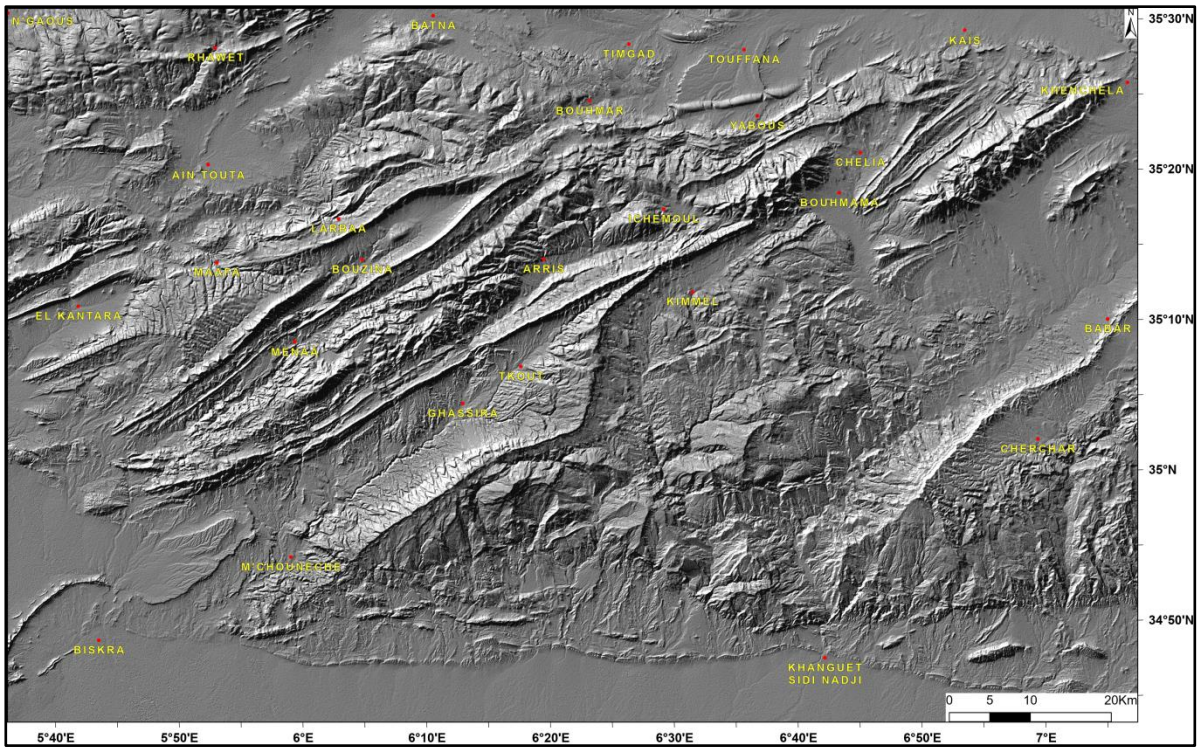

Fig. 5 Grey shaded relief derived from SRTM data with 135° solar azimuth

Lineament extraction was performed using automatic and manual approaches. The automatic technique was accomplished using the LINE algorithm of PCI Geomatica software on the four directional filters ($N0^o$, $N45^o$, $N90^o$ & $N135^o$) and the shaded relief derived from SRTM data. The Line module extracts linear features from images and generates polyline shapefiles using six adjusting parameters.

For the manual technique, ArcGIS software was used. The layers obtained from the processing phase (Band combinations, band ratios, PCA, directional filters, and shaded reliefs) in addition to the georeferenced and digitized geological map (Fig. 2), were superimposed. Each layer was turned visible at once, and apparent lineaments were drawn using the polyline tool. This superimposition technique allowed us to trace the lineaments and validate them through multiple layers. Both automatic and manual extracted lineaments were grouped into one layer for analysis and discussion (Fig. 6).

Results and Discussion

The application of the mentioned techniques on multiple superimposed layers allowed the drawing of the Aures Massif synthetic lineament map (Fig. 6). The figure shows a population of 12,702 identified and validated lineaments of varying lengths and directions (6,591 extracted automatically and 6,111 manually). Sentinel-2 images allow extracting more lineaments than other satellite images, while the lineaments obtained from SRTM data are the most significant for our study.

Length and orientation: Lineaments' length varies between 0.02 km and 13.5 km, with a mean of 1.43 km and a standard deviation of 1.035 km. The total length is 18,176 km, whereas most lineaments (90%) are less than 2.59 km long (Fig. 7). The longest lineament (13.5 km) is located at the north-eastern part of Djebel Azreg, corresponding to an important NE-SW directional fault that separates Aptian lands from Albian ones.

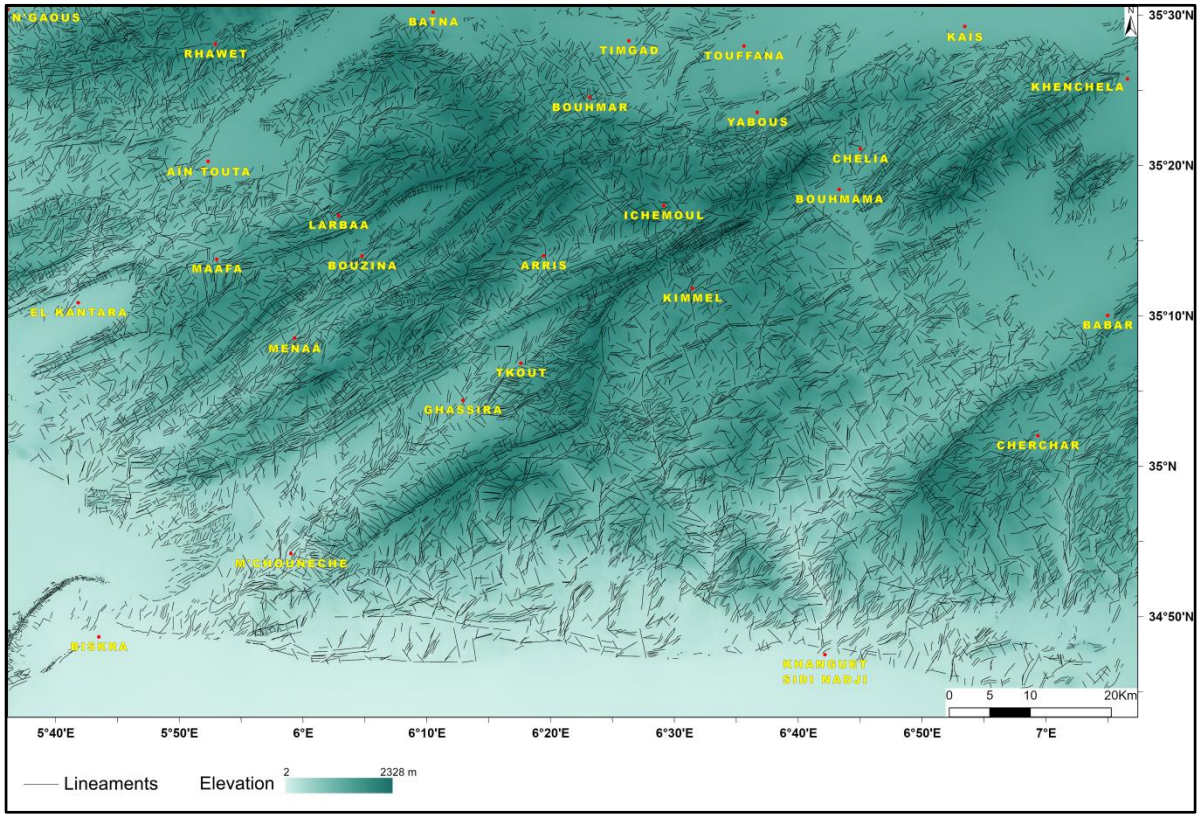

Fig. 6 Synthetic lineament map of the Aures Massif

Mapped lineaments are grouped into eighteen classes with an interval of 10°. The number of lineaments, the total length, and the percentage of the latter two were calculated for each class and given in Fig. 8a. The rose diagram of the extracted lineaments is given in Fig. 8b. The last enables an easy overview of the general lineaments' disposition orientations. Four major sets are recognizable, oriented NE-SW, NW-SE, E-W, and N-S. The NE-SW lineaments are the most dominant with a percentage of 58.80 % and a total length of 11826.1 km; the NW-SE orientation form the second most family with a percentage of 24.44% and a total length of 3,628.37 km; the E-W family has a percentage of 9.93% and a total length of 1,651.38 km, the N-S family is of less importance and represented by 867 lineaments with a percentage of 6.83%.

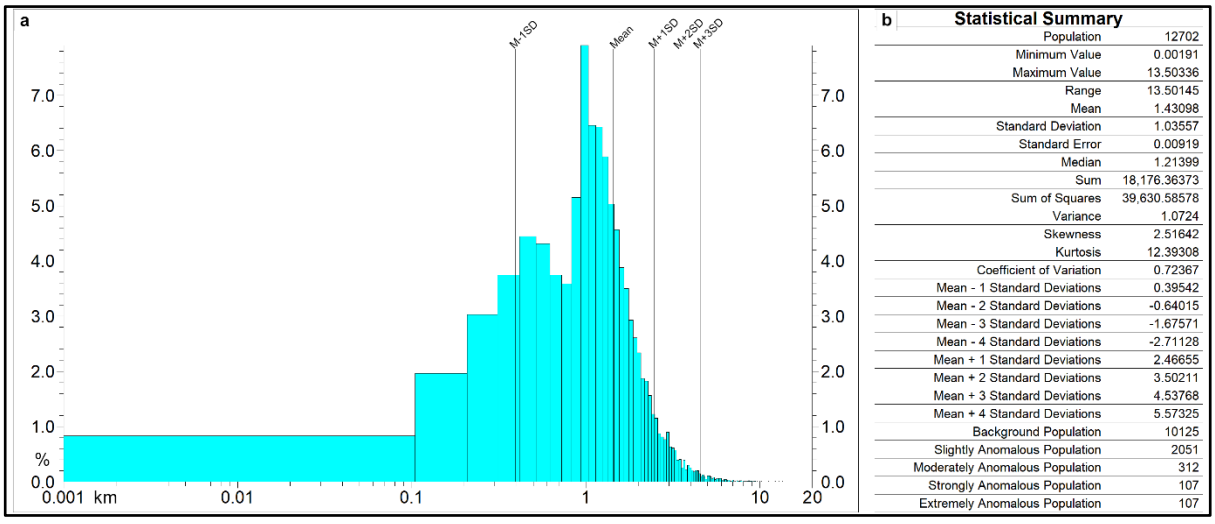

b **Statistical Summary**

Population	12702
Minimum Value	0.00191
Maximum Value	13.50336
Range	13.50145
Mean	1.43098
Standard Deviation	1.03557
Standard Error	0.00919
Median	1.21399
Sum	18,176.36373
Sum of Squares	39,630.58578
Variance	1.0724
Skewness	2.51642
Kurtosis	12.39308
Coefficient of Variation	0.72367
Mean - 1 Standard Deviations	0.39542
Mean - 2 Standard Deviations	-0.64015
Mean - 3 Standard Deviations	-1.67571
Mean - 4 Standard Deviations	-2.71128
Mean + 1 Standard Deviations	2.46655
Mean + 2 Standard Deviations	3.50211
Mean + 3 Standard Deviations	4.53768
Mean + 4 Standard Deviations	5.57325
Background Population	10125
Slightly Anomalous Population	2051
Moderately Anomalous Population	312
Strongly Anomalous Population	107
Extremely Anomalous Population	107

Fig.7 a Frequency histogram of lineament lengths (semi-loggraph)
b Basic statistics of lineament lengths

The combined analysis of length and frequency reveals that NW-SE lineaments have the highest length average, in contrast, the NE-SW lineaments have the lowest average (Table 3).

Density: The analysis of lineament density is a commonly used parameter in the interpretation of lineaments' concentration and distribution (Adiri et al., 2017; Bonetto et al., 2015; Javhar et al., 2019; Lachaine, 1999; Pinto et al., 2017). The present study uses density to understand the relationship between lineaments' distribution and its controlling factors.

a

Class (°)	Count	Percentage (%)	Total length (km)	Length percentage (%)
[0-10]	423	3.33	543.51	2.99
[10-20]	615	4.84	812.48	4.47
[20-30]	782	6.16	1091.57	6.01
[30-40]	1075	8.46	1632.57	8.98
[40-50]	1338	10.53	2136.59	11.75
[50-60]	1499	11.80	2600.93	14.31
[60-70]	1340	10.55	2205.47	12.13
[70-80]	985	7.75	1577.87	8.68
[80-90]	668	5.26	882.72	4.86
[90-100]	451	3.55	564.89	3.11
[100-110]	348	2.74	410.26	2.26
[110-120]	375	2.95	422.77	2.33
[120-130]	487	3.83	530.28	2.92
[130-140]	513	4.04	595.21	3.27
[140-150]	596	4.69	712.74	3.92
[150-160]	513	4.04	630.91	3.47
[160-170]	358	2.82	426.41	2.35
[170-180]	336	2.65	399.18	2.20

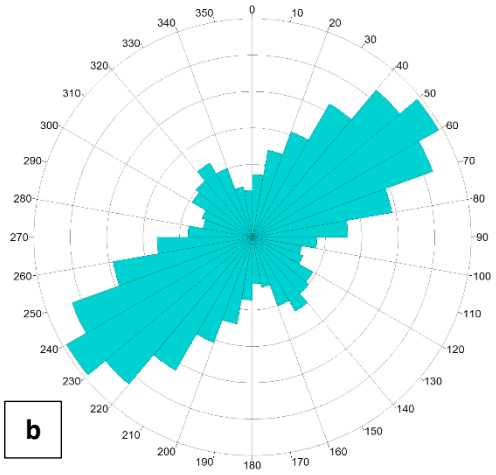

b

Fig. 8 a Basic statistics of lineaments' direction classes **b** Rose diagram of extracted lineaments

Table 3 Lineaments orientation sets

Orientation	Number	Frequency (%)	Total length (km)	Total length/Number (km)
NE-SW	7469	58.80	11826.1	1.58
NW-SE	3104	24.44	3628.37	1.17
E-W	1262	9.93	1651.38	1.31
N-S	867	6.83	1070.51	1.23

The Aures Massif lineaments' density map (Fig. 9) was obtained using the line density tool in ArcGIS. From the observation of the Aures Massif density map (Fig. 12), one can observe that the different lineaments are not evenly distributed throughout the study area. Generally, the high-density areas are localized in the northwestern portion of the map, with the most concentration along the anticline axis of Dj. Azereg-Djebel Ichemoul-Djebel Chélia and the Ghassira syncline. The earlier is considered the center of the Aures basin by many authors (Ghandriche, 1991; Herkat, 1999; Laffite, 1939; Yahiaoui, 1990). South-eastward, the density decreases except in some localized areas in Djebel Taktiout and Djebel Toubount showing moderate to high density. The Paleogene of Ghassira syncline often has the highest density in the whole Aures.

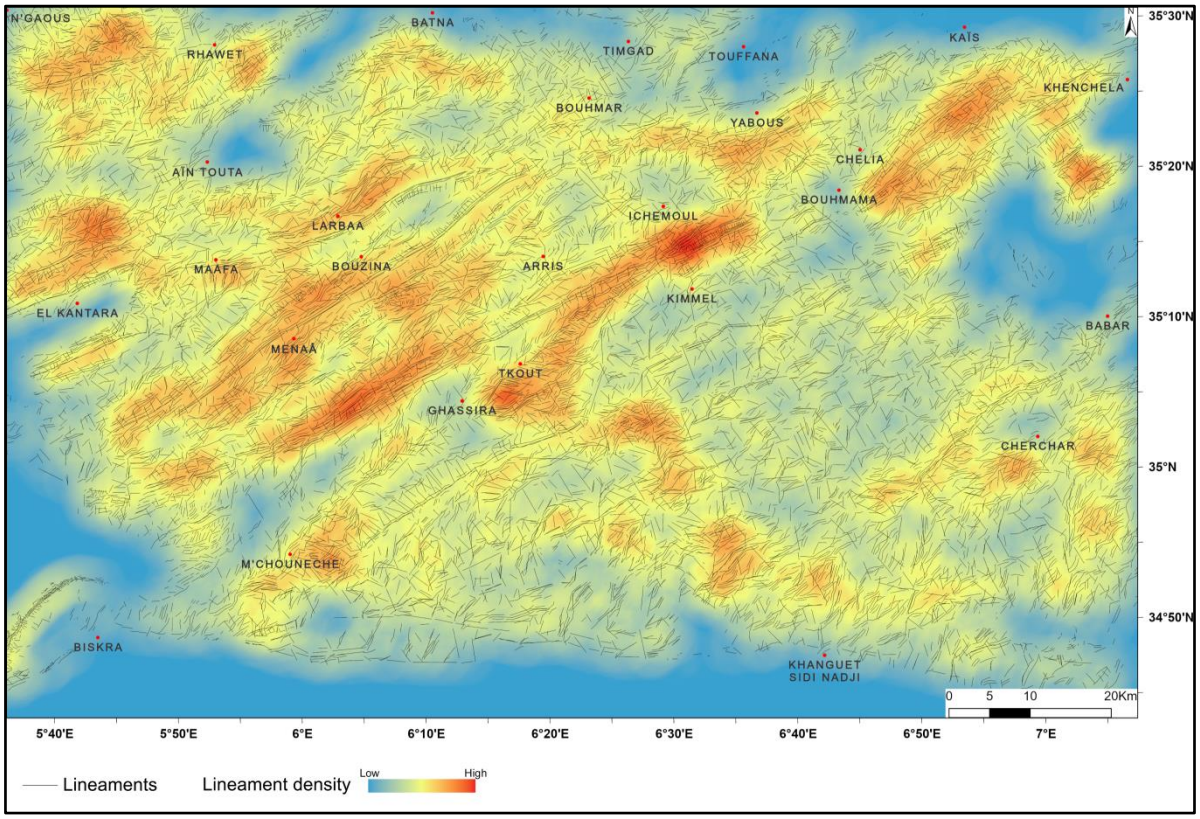

Fig.9 Lineament density map of the Aures Massif

Distribution controlling factors: The distribution and the localization of the lineaments are controlled by various factors which can be grouped into topographic and geological factors.

Topographic factors: The slope image is derived from SRTM data using the slope tool in ArcGIS. The superposition of the density map (Fig. 9) on the slope image (Fig. 10) shows a clear concordance between the two, where areas with high lineament densities correspond to areas with the highest variation of elevation.

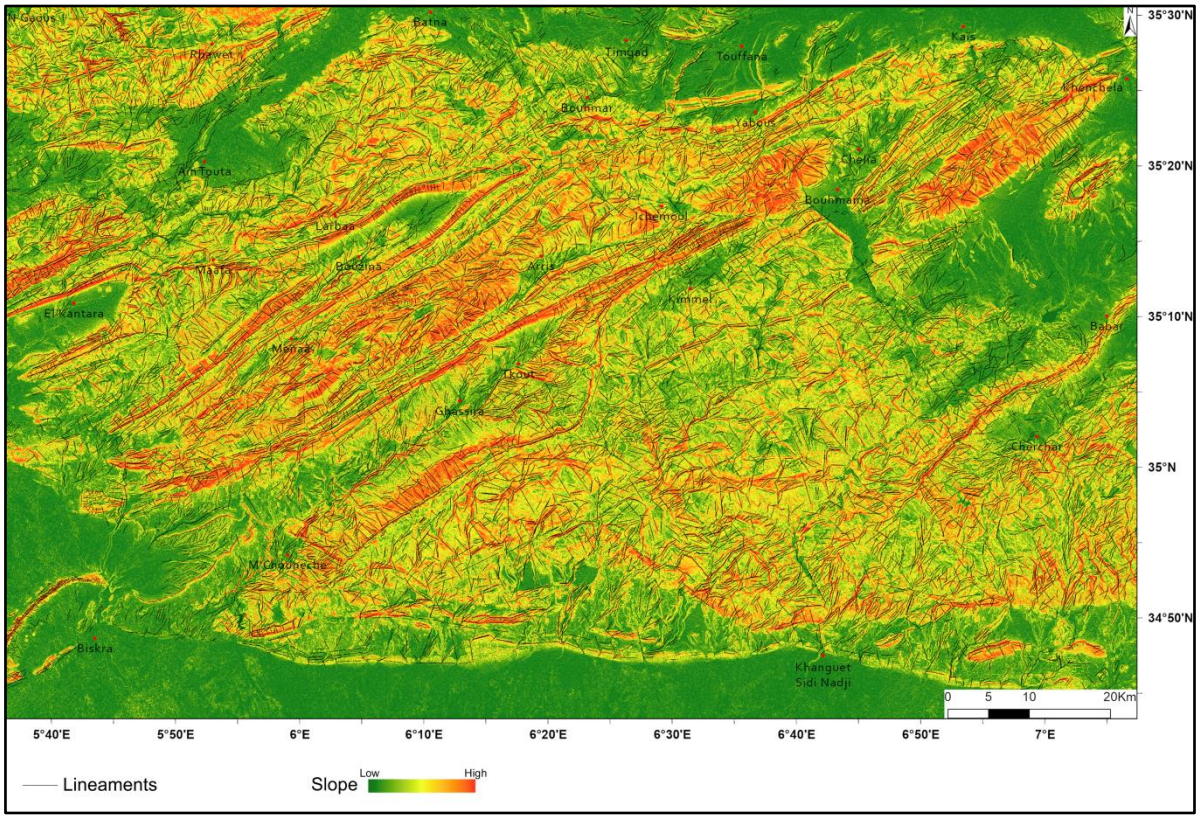

Fig.10 Superposition of the lineaments on the slope map of the Aures

Geological factors: The superposition of the obtained density map on the geologic map shows that the Lower Cretaceous, the Maastrichtian, and the Paleogene formations have the most densities; these stages contain competent rocks that show brittle behavior during compressions and which reflect the highest densities. In contrast, the Neogene formations are the least affected areas and this is due to their high content of clays and their recent age. Another observation is that high-density areas often align with major fault corridors.

Structure: The combined use of remote sensing and GIS to extract lineaments allowed us to discern the linear proprieties and conclude the structural features of the Aures.

The NE-SW direction set forms the most abundant direction in the Aures Massif. The lineaments of this set correspond to the big fold axes generated by the Atlasic tectonic phase and to directional faults. In a regional frame, the Souk Ahras-Batna NE-SW fault manifests by putting in contact Miocene with the Turonian of Djebel Ich Ali's northern flank (Glangeaud, 1951).

The NE-SW direction set is present in the study area with lengths going generally from small to average. The kinematic corresponds mostly to dextral strike-slip faults. Lineaments belonging to this direction are met all over the Aures massif and of which the most remarkable one is located between the tip of Djebel Metlili and Sidi Khelil (Guiraud, 1973).

E-W direction set: The lineaments of this set are less numerous and of less importance. They correspond most often to structures of the Miocene age at the NE limit of the Aures massif as well as to the South Saharan Flexure at the Southern limit of the Massif.

The N-S family is sometimes found in the mapped region with a generally local extension. These lineaments most often correspond to accidents generated by the Alpine phase.

CONCLUSION

Remote sensing has shown its efficiency in the structural mapping of the Aures Massif. The latter covers a big area with remote locations, where traditional methods make mapping challenging. The methodology adopted in this study consisted of four steps starting from data gathering by downloading different image sets; we relied on three types of satellite images: Landsat 9, Sentinel 2-A, and SRTM data for their proven lineament extraction performance. The second step is to preprocess the data by applying geometric and atmospheric corrections. The obtained images were later processed by applying multiple visual technics depending on the dataset type, whether multispectral (Landsat and Sentinel) or Digital Elevation Model (SRTM DEM). The final step is to extract lineaments; in our study, both manual and automatic extraction methods were applied on more than twenty layers for maximum significant structural lineaments. The produced lineament map accompanied by statistical analysis shows that the study area is cross-cut by a dense lineament network where four lineament sets were discerned: NW-SE, NE-SW, E-W, and N-S.

The geologic factors represented in the rock's competency and age controlled the lineament

distribution. Another controlling factor is topography, where places with rapid slope change form the area's most dense parts.

The comparison with available geological data shows that these structural lineaments correspond mainly to faults resulting from the succession of multiple tectonic phases. The most important phases responsible for the structuration of the Aures are the most recent ones that took place during the Tertiary during the Alpine orogeny.

ACKNOWLEDGMENTS

Without the free access to datasets provided by USGS this work won't ever see the light. We would also thank the anonymous reviewers for reviewing this contribution.

REFERENCE

Abdelouhed, F., Ahmed, A., Abdellah, A., Mohammed, I., and Zouhair, O. 2022. Extraction and analysis of geological lineaments by combining ASTER-GDEM and Landsat-8 image data in the central High Atlas of Morocco. Natural Hazards, 111(2), 1907-1929. https://doi.org/10.1007/s11069-021-05122-9

Adepoju, M. O., Odeyemi, I. B., and Akinluyi, F. O. 2021. Landsat-8 lineament analysis for detection of epigenetic mineralization zones in parts of Igarra Schist Belt, Southwestern Nigeria. Remote Sensing in Earth Systems Sciences, 4(1), 76-86. https://doi.org/10.1007/s41976-021-00046-1

Adhab, S. S. 2014. Lineament automatic extraction analysis for Galal Badra river basin using Landsat 8 satellite image. Iraqi Journal of Physics, 12(25), 44-55. https://doi.org/10.30723/ijp.v12i25.303

Adiri, Z., El Harti, A., Jellouli, A., Lhissou, R., Maacha, L., Azmi, M., Zouhair, M., and Bachaoui, E. M. 2017. Comparison of Landsat-8, ASTER and Sentinel 1 satellite remote sensing data in automatic lineaments extraction: A case study of Sidi Flah-Bouskour inlier, Moroccan Anti Atlas. Advances in space research, 60(11), 2355-2367. https://doi.org/10.1016/j.asr.2017.09.006

Ahmadi, H. and Pekkan, E. 2021. Fault-based geological lineament extraction using remote sensing and GIS—a review. Geosciences, 11(5), 183. https://doi.org/10.3390/geosciences11050183

Al-Saedi, Z. J. 2013. Lineament extraction for assessment of groundwater potential/West of Iraq. Euphrates Journal of Agriculture Science, 5(1), 54-63. https://doi.org/10.13140/RG.2.2.24225.53607

Benabbas, C. 2006. Evolution mio-Plio-Quaternaire des bassins continentaux de l'Algerie nord orientale [Mio-Plio-Quaternary evolution of continental basins of NE Algeria] Université Mentouri-Constantine-]. https://bu.umc.edu.dz/theses/sc-terre/BEN4532.pdf

Benmansour, S., Yahiaoui, A. and Kechid-Benkherouf, F. 2018. Le Campanien-Maastrichtien du bassin des Aurès, Algérie : biostratigraphie, paléoenvironnements et leurs implications. Annales de Paléontologie, 104(1), 1-26. https://doi.org/https://doi.org/10.1016/j.annpal.2017.11.001

Bensekhria, A., Marmi, R. and Yahiaoui, A. 2019. Cenomanian and lower Turonian relative chronology and palaeoenvironmental framework of the Nouader site (Aures Basin, Northeastern Algeria). Geological Magazine, 156(11), 1877-1891. https://doi.org/10.1017/S0016756819000153

Bentahar, I., Raji, M., and Si Mhamdi, H. 2020. Fracture network mapping using Landsat-8 OLI, Sentinel-2A, ASTER, and ASTER-GDEM data, in the Rich area (Central High Atlas, Morocco). Arabian Journal of Geosciences, 13(16), 1-19. https://doi.org/10.1007/s12517-020-05736-6

Bonetto, S., Facello, A., Ferrero, A. M. and Umili, G. 2015. A tool for semi-automatic linear feature detection based on DTM. Computers and Geosciences, 75, 1-12. https://doi.org/10.1016/j.cageo.2014.10.005

Bouillin, J.-P. 1986. Le "bassin Maghrebin"; une ancienne limite entre l'Europe et l'Afrique a l'ouest des Alpes. Bulletin de la Société Géologique de France, 2(4), 547-558.

Bruning, J. N., Gierke, J. S. and Maclean, A. L. 2011. An approach to lineament analysis for groundwater exploration in Nicaragua. Photogrammetric Engineering and Remote Sensing, 77(5), 509-519. https://doi.org/10.14358/PERS.77.5.509

Canty, M. J. 2014. Image analysis, classification and change detection in remote sensing: with algorithms for ENVI/IDL and Python (3rd ed.). Crc Press.

Chuvieco, E. 2020. Fundamentals of Satellite Remote Sensing: An Environmental Approach (3rd ed.). CRC Press. https://doi.org/10.1201/9780429506482

Djaiz, F. 2011. Le bassin néogène de Timgad : études sédimentaire et tectonique (Algérie nord-orientale) Université des Frères Mentouri Constantine]. https://bu.umc.edu.dz/theses/sc-terre/DJA6068.pdf

Domzig, A. 2006. Déformation active et récente, et structuration tectonosédimentaire de la marge sous-marine Algérienne Université de Bretagne occidentale-Brest]. https://tel.archives-ouvertes.fr/docs/00/14/46/84/PDF/these_Domzig.pdf

Drury, S. 2001. Image interpretation in Geology (3rd ed.). Blackwell Science.

.

Durand Delga, M. 1969. Focus on the structure of the NE of the Barbary. Bull. Serv. Map. Geol., Algeria, 39, 89-131.

Fossi, D. H., Dadjo Djomo, H., Takodjou Wambo, J. D., Ganno, S., Pour, A. B., Kankeu, B. and Nzenti, J. P. 2021. Structural lineament mapping in a sub-tropical region using Landsat-8/SRTM data: a case study of Deng-Deng area in Eastern Cameroon. Arabian Journal of Geosciences, 14(23), 1-22. https://doi.org/10.1007/s12517-021-08848-9

Ghandriche, H. 1991. Modalités de la superposition de structures de plissement-chevauchement d'âge alpin dans les Aurès (Algérie). Orsay, France: Univ. Paris XI Sud.

Glangeaud, L., 1951. Interprétation tectono-physique des caractères structuraux et paléogéographiques de la Méditerranée occidentale. Bulletin de la Société géologique de France, 6(8), 735-762. https://doi.org/10.2113/gssgfbull.S6-I.8.735

Guiraud, R., 1973. Evolution post-triasique de l'avant-pays de la chaîne alpine en Algérie Toulouse].

Herkat, M. 1999. La Sédimentation de haut niveau marin du cretacé supérieur de l'Atlas Saharien oriental et des Aurès University of Algiers USTHB, Algeria, 802 pp. Published PhD thesis

Hobbs, W. H. 1904. Lineaments of the Atlantic border region. Bulletin of the Geological Society of America, 15(1), 483-506. https://doi.org/10.1130/GSAB-15-483

Hobbs, W. H. (1912). Earth features and their meaning; an introduction to geology for the student and the general reader. Macmillan, New York, p.506. https://doi.org/10.5962/bhl.title.18732

Hubbard, B. E., Mack, T. J. and Thompson, A. L. 2012. Lineament analysis of mineral areas of interest in Afghanistan: Automatically delineated lineaments using 30-m TM imagery. U.S. Geological Survey Open-File Report, 1084, 28. http://pubs.usgs.gov/of/2012/1048

Hung, L., Batelaan, O. and de Smedt, F. 2005. Lineament extraction and analysis, comparison of LANDSAT ETM and ASTER imagery. Case study: Suoimuoi tropical karst catchment, Vietnam. Remote Sensing for Environmental Monitoring, GIS Applications, and Geology V, Remote sensing for environmental monitoring, GIS applications, and geology V: 19-20 September 2005, Bruges, Belgium (Proceedings of SPIE - The International Society for Optical Engineering; Vol. 5983). SPIE. https://doi.org/10.1117/12.627699

Javhar, A., Chen, X., Bao, A., Jamshed, A., Yunus, M., Jovid, A. and Latipa, T. 2019. Comparison of multi-resolution optical Landsat-8, Sentinel-2 and Radar Sentinel-1 data for automatic lineament extraction: A case study of Alichur area, SE Pamir. Remote Sensing, 11(7), 778. https://doi.org/10.3390/rs11070778

Khalifa, A., Bashir, B., Çakir, Z., Kaya, Ş., Alsalman, A. and Henaish, A. 2021. Paradigm of geological mapping of the Adıyaman Fault Zone of Eastern Turkey using Landsat 8 remotely sensed data coupled with PCA, ICA, and MNFA techniques. ISPRS International Journal of Geo-Information, 10(6), 368. https://doi.org/10.3390/ijgi10060368

Lachaine, G. 1999. Structures géologiques et linéaments, Beauce (Québec}: apport de la télédétection University of Sherbrooke Québec, Québec. https://www.bac-lac.gc.ca/eng/services/theses/Pages/item.aspx?idNumber=1006674468

Laffite, R. 1939. Etude de géologie de l'Aurès. Doctorat ès Sciences Paris. Bull. Serv. Carte Géol. Algérie, 1re série(15), 484.

Liu, C. C., Sousa Jr, M. d. A. and Gopinath, T. R. 2000. Regional structural analysis by remote sensing for mineral exploration, Paraiba State, Northeast Brazil. Geocarto International, 15(1), 70-77. https://doi.org/10.1080/10106040008542142

Mwaniki, M. W., Matthias, M. S., and Schellmann, G. 2015. Application of remote sensing technologies to map the structural geology of central Region of Kenya. IEEE Journal of Selected Topics in Applied Earth Observations and Remote Sensing, 8(4), 1855-1867. https://doi.org/10.1109/JSTARS.2015.2395094

O'Leary, D., Friedman, J. and Pohn, H. 1976. Lineament, linear, lineation: some proposed new standards for old terms. Geological Society of America Bulletin, 87(10), 1463-1469. https://doi.org/10.1130/0016-7606(1976)87%3C1463:LLLSPN%3E2.0.CO;2

Pinto, D., Shrestha, S., Babel, M. S. and Ninsawat, S. 2017. Delineation of groundwater potential zones in the Comoro watershed, Timor Leste using GIS, remote sensing and analytic hierarchy process (AHP) technique. Applied Water Science, 7(1), 503-519. https://doi.org/10.1007/s13201-015-0270-6

Ramli, M., Yusof, N., Yusoff, M., Juahir, H., and Shafri, H. 2010. Lineament mapping and its application in landslide hazard assessment: a review. Bulletin of Engineering Geology and the Environment, 69(2), 215-233. https://doi.org/10.1007/s10064-009-0255-5

Raoult, J.-F., 1974. Geologie du Centre de la Chaine Numidique (Nord Du Constantinois, Algerie). Mémoire Société Géologique Français.,N.S.,t.III n° 121,164p., 11pl.h.t.

Saint Jean Patrick Coulibaly, H., Talnan Jean Honoré, C., Naga, C., Claude Alain Kouadio, K., Régis Mailly DIDI, S., Diedhiou, A. and Savane, I. 2020. Groundwater exploration using extraction of lineaments from SRTM DEM and water flows in Béré region. https://doi.org/10.1016/j.ejrs.2020.07.003

Salui, C. L. 2018. Methodological validation for automated lineament extraction by LINE method in PCI Geomatica and MATLAB-based Hough transformation. Journal of the Geological Society of India, 92(3), 321-328. https://doi.org/10.1007/s12594-018-1015-6

Soliman, A. and Han, L. 2019. Effects of vertical accuracy of digital elevation model (DEM) data on automatic lineaments extraction from shaded DEM. Advances in space research, 64(3), 603-622. https://doi.org/10.1016/j.asr.2019.05.009

Tzvetkov, J. 2018. Relief visualization techniques using free and open source GIS tools. Polish Cartographical Review, 50. https://doi.org/10.2478/pcr-2018-0004

Yahiaoui, A. 1990. La partie inférieure de la série marno-calcaire du Crétacé supérieur (Cénomanien supérieur à Coniacien inférieur) entre Batna et El Kantara (Algérie orientale): Stratigraphie, Sédimentologie et Paléogéographie Université Henri Poincaré-Nancy 1].